Computer Assisted Mechanics and Engineering Sciences, 5: 227–243, 1998.

An aspect ratio condition for the buckling and folding of polymeric jets in injection mould filling

Nawaz Mahomed and Michał Kleiber
Centre for Research in Applied Technology, Peninsula Technikon, P.O. Box 1906, Bellville 7535, South Africa
Institute of Fundamental Technological Research, Polish Academy of Sciences, Świętokrzyska 21, 00-049 Warsaw, Poland

(Received November 21, 1997)

The behaviour of planar Newtonian and Non-Newtonian polymeric jets is investigated in the context of injection mould filling. The incompressible Stokes flow model consistent with the application of injection mould filling is described together with the shear rate dependent fluid viscosity for a typical polymeric melt. The numerical procedure for the solution of the nonlinear system is briefly discussed as well as the mesh generation and the melt front tracking algorithms employed.

In the analysis, the buckling behaviour of Newtonian and Non-Newtonian jets are firstly compared. Thereafter the behaviour of Newtonian jets are analysed for various values of the aspect ratio in an attempt to study the validity of the Cruikshank buckling conditions for planar Newtonian jets. It is argued that the Reynolds number of highly viscous polymeric melts is relatively low and the aspect ratio condition is the critical condition dictating the buckling behaviour. Finally, an aspect ratio design criteria is established for buckling-free and folding-free flow of polymeric jets.

Keywords: Injection moulding, free surface flows, unsteady Non-Newtonian flow

1. Introduction

Jetting of polymeric melts may occur in the injection mould filling process, especially when the melt enters the gate of the mould or when it enters mould cavity chambers via narrow constrictions. The jetting behaviour cannot be modelled by the Hele-Shaw flow model which is used widely in commercial applications of injection moulding of thin parts. The reason is that the potential flow model produces an equipotential free surface which requires slip along the solid boundaries. The resulting free surface is too inaccurate to model the jetting phenomenon. Furthermore, most commercial applications employ an Eulerian formulation in which the finite element mesh is fixed to the domain. The free surface is then tracked using techniques such as the control volume approach, resulting in further inaccuracies in the free surface position.

Many researchers, as reviewed by Tomé *et al.* [13], have produced experimental evidence predicting the buckling of thin viscous jets hitting a rigid plate. However, a rigorous two-dimensional theory for this behaviour has yet to be established. Nevertheless, certain criteria based on experimental and approximate theoretical results have been developed for the prediction of buckling of planar viscous jets. In particular, Cruikshank [5] has proposed that buckling will occur if the following restrictions are satisfied:

$$\mathrm{Re} < 0.56 \quad \text{and} \quad H/D > 3\pi$$

where Re is the Reynolds number based on the gate width D, and H is the height of the gate above the normal obstruction.

In the case of Newtonian behaviour, the Reynolds number can easily be established. However, in injection mould filling where highly viscous polymer melts flow with considerable shearing, the Non-Newtonian behaviour in which the viscosity is a function of the shear-rate cannot be ignored. This

makes the Reynolds number vary locally and is therefore difficult to establish effectively. However, it will be shown that, for typical polymeric melts, the Reynolds number is extremely small and, even for very high shear-rates, satisfies the above condition locally. The aspect ratio condition is therefore the critical or deciding condition affecting the buckling of polymeric jets.

Whilst the Cruikshank conditions dictate the buckling of planar viscous jets, they do not take account of the folding of the free surface. Folds may occur, especially in the case of highly viscous polymeric melts, even in the absence of buckling. The phenomena of buckling and folding are undesirable in the injection mould filling process. They result in numerous weld lines in the moulded part which lead to reduced part strength. The aim is therefore to establish a suitable aspect ratio condition which may be used in the design of injection moulds to prevent the buckling and folding of polymeric jets. At the same time, the validity of the Cruikshank conditions for highly viscous (Stokesian) flow will be investigated.

The computational simulation of the buckling of planar jets has been investigated by Tomé *et al.* [13], but for relatively high Reynolds number. The buckling of low Reynolds number jets was simulated by Ken-ichiro Mori *et al.* [11], but for the application of metal injection moulding. Although the latter is close to the application of polymer injection moulding, no clear design criteria were provided for the avoidance of buckling.

2. THE PROBLEM FORMULATION

2.1. The flow formulation

The principle of conservation of momentum applied to a general fluid continuum yields the Navier-Stokes equation:

$$\frac{\partial}{\partial t}\rho\mathbf{v} = (\mathbf{v}\cdot\nabla)\rho\mathbf{v} - \nabla p - \nabla\cdot\boldsymbol{\tau} + \rho\mathbf{g} \tag{1}$$

where $\mathbf{v}$ is the velocity vector, p the hydrostatic pressure, $\boldsymbol{\tau}$ the stress tensor, ρ the fluid density, and $\mathbf{g}$ the gravitational acceleration vector. Since most injection moulding applications involve the moulding of thin sections, use of a two-dimensional model is sufficient in which the velocity vector is described as $\mathbf{v} = v_i\mathbf{e}_i$, $\mathbf{i} = 1, 2$, where $\mathbf{e}_i$ is the unit vector in the ith component direction. The assumption of incompressible Stokesian flow with no gravitational influence is also consistent with the physical problem of mould filling, as is that of isothermal conditions. The equation for steady state flow therefore reduces to:

$$\nabla\cdot\boldsymbol{\pi} = 0 \tag{2}$$

where the total stress tensor $\boldsymbol{\pi}$ is given by

$$\boldsymbol{\pi} = p\boldsymbol{\delta} + \boldsymbol{\tau} \tag{3}$$

where δ is the unit tensor. For Generalised Newtonian flow, the constitutive equation relating the stress τ to the rate of deformation tensor $\dot{\gamma}$ for incompressible flow is

$$\boldsymbol{\tau} = -2\eta\dot{\boldsymbol{\gamma}}, \tag{4}$$

where

$$\dot{\boldsymbol{\gamma}} = \frac{1}{2}\left[\nabla\mathbf{v} + (\nabla\mathbf{v})^{\mathrm{T}}\right]. \tag{5}$$

Also, the viscosity η is a function of the scalar deformation rate $\dot{\gamma}_s$, the latter defined as the scalar invariant $\sqrt{2\dot{\boldsymbol{\gamma}} : \dot{\boldsymbol{\gamma}}}$ which gives

$$\dot{\gamma}_s = \left[\left(\frac{\partial v_1}{\partial x_2}\right)^2 + \left(\frac{\partial v_2}{\partial x_1}\right)^2 + \left(\frac{\partial v_1}{\partial x_1} + \frac{\partial v_2}{\partial x_2}\right)^2 + \left(\frac{\partial v_1}{\partial x_1}\right)^2 + \left(\frac{\partial v_2}{\partial x_2}\right)^2\right]^{1/2}. \tag{6}$$

In addition to Eq. (1), the incompressibility condition

$$\nabla \cdot \mathbf{v} = 0 \tag{7}$$

must also be satisfied.

2.2. Boundary conditions

The boundary Γ of the domain Ω is subdivided into non-overlapping subsets Γ_e, Γ_w and Γ_f, as shown in Fig. 1, with boundary conditions:

$$\mathbf{v} = \mathbf{v}_e \qquad \text{on } \Gamma_e \quad \text{(entrance boundary)} \tag{8}$$

$$\mathbf{v} = 0 \qquad \text{on } \Gamma_w \quad \text{(non-slip boundary)} \tag{9}$$

$$\left.\begin{aligned} \boldsymbol{\pi}_n \cdot \mathbf{n} &= \frac{\sigma}{R(\Gamma_f)} \\ \boldsymbol{\pi}_n \cdot \mathbf{t} &= 0 \end{aligned}\right\} \quad \text{on } \Gamma_f \quad \text{(free surface boundary)} \tag{10}$$

where $\boldsymbol{\pi}_n$ denotes the total stress vector on a plane normal to the boundary. The vectors $\mathbf{n}$ and $\mathbf{t}$ are the unit normal and tangential vectors on the free surface, σ is the surface tension coefficient, and R is the radius of curvature of the free surface which can be found using

$$\frac{1}{R(\Gamma_f)} = \left|\frac{\mathrm{d}t}{\mathrm{d}\Gamma_f}\right|$$

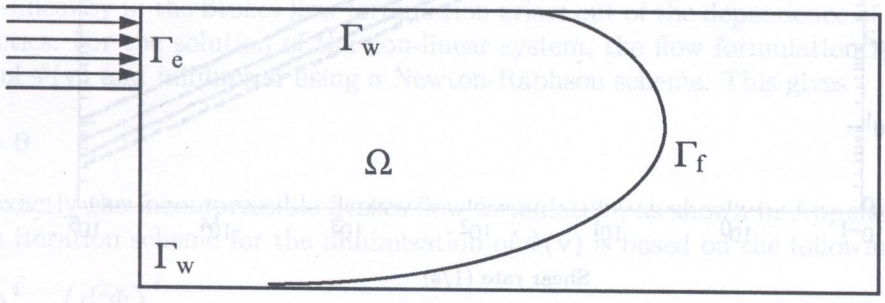

Fig. 1. Illustration of the boundaries in the injection moulding filling process

The kinetic energy of the fluid flowing across the free surface boundary is given by the following expression:

$$\int_{\Gamma_f} \frac{1}{2}\rho|\mathbf{v}|^2 \mathbf{v} \cdot \mathbf{n}\mathrm{d}\Gamma \,.$$

On the other hand, the energy in the free surface which acts as a resistance to the outflow of the free surface fluid particles can be called the strain energy due to surface tension. This is given by the expression:

$$\int_{\Gamma_f} \frac{\sigma}{R(\Gamma_f)} \mathbf{v} \cdot \mathbf{n}\mathrm{d}\Gamma \,.$$

Owing to the high velocities prevalent in the type of unsteady flow problem considered here, the kinetic energy of the free surface particles is much higher than the strain energy due to surface tension, as can be seen by the form of the above two expressions. The influence of the surface tension on the form of the free surface is therefore negligible. This results in the assumption of zero stress vector, or traction, on the free surface boundary. All models on injection moulding referenced in this study employ this assumption. In fact, Tomé *et al.* [40] refer to an "absence" of surface tension.

The boundary conditions (8)–(10) are sufficient to solve the flow formulation with explicit time integration for the advancement of the free surface.

2.3. Material characterisation

In the mould filling process, the Non-Newtonian behaviour of the polymer melt is characterised by the viscosity dependence on various flow conditions. These conditions are as follows: the shear rate $\dot{\gamma}_s$, the fluid temperature T, and the fluid pressure p. In addition to this, the temperature and pressure also depend on the fluid density (or specific volume), but this dependence may be neglected because of the incompressibility of the polymer melt during the filling stage. Polymer melts generally exhibit a shear thinning behaviour, as depicted by the rheological curves in Fig. 2, and this can be well represented by the following Cross-type model:

$$\eta(\dot{\gamma}_s, T, p) = \frac{\eta_0(T,p)}{1 + \left(\dfrac{\eta_0 \dot{\gamma}_s}{\tau^*}\right)^{1-n}} \,. \tag{11}$$

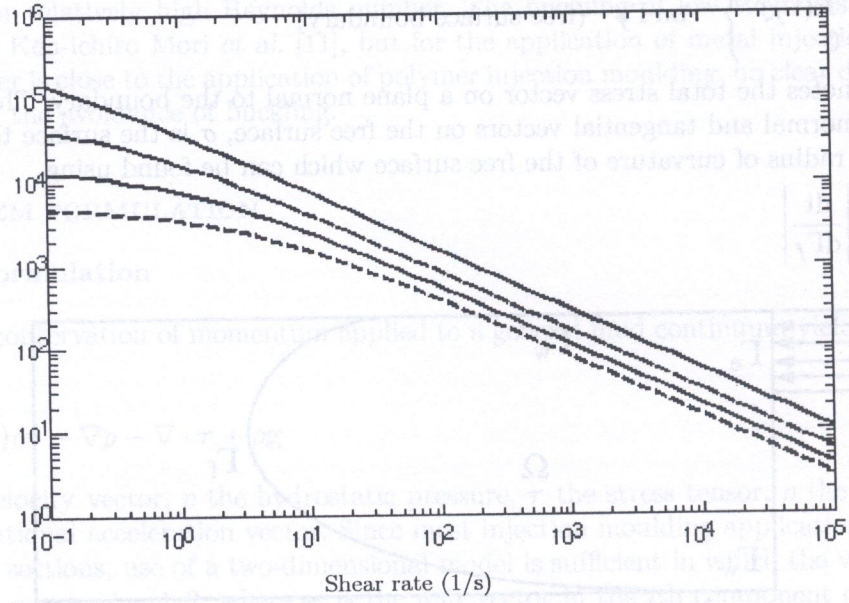

Fig. 2. Viscosity versus shear rate profile for the polystyrene grade Dow Styron 685 (from the resin database of C-MOLD Injection Moulding Simulation Software)

Here, η_0 represents the viscosity at zero shear rate, n corresponds to the power-law index, and τ^* represents the shear stress level of the transition region between the Newtonian and power-law asymptotic limits. All these parameters can be derived from rheological data obtained experimentally by viscometric analysis. A set of rheological curves obtained by viscometric analysis is shown in Fig. 2 for a particular material.

For large values of n, the Cross model can be shown to reduce to the more familiar power-law model:

$$\eta(\dot{\gamma}_s, T, p) = m(T,p)(\dot{\gamma}_s)^n \,.$$

Perhaps the simplest accurate representation of $\eta_0(T,p)$ is in terms of an Arhenius-type temperature sensitivity and pressure dependence such as

$$\eta_0(T,p) = B \exp\left(\frac{T_b}{T}\right) \exp(\beta p) \,. \tag{12}$$

In this case, Eqs. (11) and (12) represent a five constant $(n, \tau^*, B, T_b, \beta)$ model for $\eta(\dot{\gamma}_s, T, p)$, also known as the Cross-Exponential viscosity model. For the filling stage, the fluid pressure is relatively low and Eq. (12) may be reduced to

$$\eta_0(T, \cdot) = B \exp\left(\frac{T_b}{T}\right) \,. \tag{12a}$$

As an example, the constants for the Cross-Exponential viscosity model for Polystyrene Dow-Styron 678D, is given in the table below.

Table 1. Summary of the Cross-Exponential viscosity model constants for the Polystyrene grade Dow Styron 685 (from the resin database of C-MOLD Injection Moulding Simulation Code)

MATERIAL: PS Dow Styron 685

n	0.27988
τ^* (Pa)	1.484×10^4
B (Pa·s)	5×10^{-8}
T_b (K)	13520
β (Pa^{-1})	3.5×10^{-8}

In most injection moulding cycles, the filling stage is relatively quick so that isothermal conditions can be assumed. This means that η_0 is a constant (since T is constant) and can simply be found from the rheological curves given in Fig. 2 for a particular polymer.

3. Numerical implementation

3.1. Solution procedure for the nonlinear Stokes flow formulation

The non-linearity in the Stokes flow formulation arises out of the dependence of the viscosity on the flow kinetics. For the solution of the non-linear system, the flow formulation is posed as a convex functional $\Phi(\mathbf{v})$ and minimised using a Newton-Raphson scheme. This gives

$$\frac{\mathrm{d}\Phi}{\mathrm{d}\mathbf{v}} = \mathbf{0} \tag{13}$$

This is exactly the incompressible Stokes flow formulation, as shown in Appendix A. The Newton-Raphson iteration scheme for the minimisation of $\Phi(\mathbf{v})$ is based on the following Taylor expansion

$$\left(\frac{\mathrm{d}\Phi}{\mathrm{d}\mathbf{v}}\right)^i + \left(\frac{\mathrm{d}^2\Phi}{\mathrm{d}\mathbf{v}^2}\right)^i \Delta\mathbf{v}^i = \mathbf{0} \tag{14}$$

where i denotes the iteration count. The tangent matrix in the above equation is simply the stiffness matrix $\mathbf{K}$ in the finite element formulation of the Stokes formulation. The non-singular requirement of $\mathbf{K}$ is satisfied by the positive-definiteness of the convex functional Φ. The non-linearity does not affect the positive-definiteness nature of $\mathbf{K}$.

The Stokes formulation (2) and the incompressibility condition (7) may be posed variationally, with a penalty parameter introduced in the incompressibility condition (nearly incompressible approximation), resulting in a mixed formulation. It is, however, more convenient to substitute the pressure variable in the flow formulation with that in the penalised incompressibility condition, resulting in a single bilinear form. Four-noded quadrilateral elements with continuous bilinear velocity interpolation are used in the finite element formulation, with reduced integration of the penalty term. This scheme is equivalent to the mixed formulation using the $Q_1 - P_0$ element [7].

In the solution of Eq. (14), the velocity field is initialised as the zero shear-rate (Newtonian) velocity field $\mathbf{v}^0$. This requires the calculation of the zero shear-rate viscosity using Eq. (12a). After solving the velocity increment $\Delta\mathbf{v}^i$, the velocity field is updated according to the incremental equation

$$\mathbf{v}^{i+1} = \mathbf{v}^i + \Delta\mathbf{v}^i \,. \tag{15}$$

After the updated velocity field is calculated, the elemental shear-rates are calculated according to Eq. (6) which allows the viscosity field to be updated. The iterative process is then repeated until

the energy norm of the residual (found by multiplying the first term of Eq. (2), the residual, with the velocity field) is small enough compared to the strain energy (found by multiplying the second term of Eq. (14) with the velocity field).

3.2. Automatic mesh generation

The need for automatic mesh generators (whether quadratic or triangular) was driven largely by the introduction of adaptive mesh refinement schemes. These schemes require the regeneration of meshes during the iterative process of equalising the error distribution.

In recent years, a variety of schemes for the generation of triangular meshes were developed. Some of the most widely used schemes are those developed by Cavendish *et al.* [2] using *Delauney triangulation*, Baehmann *et al.* [1], *using the modified quadtree and modified octree* techniques, Lo [9] using the *front technique*, and Peraire *et al.* [12] using the *advancing front technique*. The main advantage of triangular mesh generation is that triangles are the easiest elements to generate in the discretisation of arbitrary shaped domains. But, in terms of the incompressible flow problem described in Sec. 2.1, the linear velocity-constant pressure triangular element shown in Fig. 3(a) violates the Babuska-Brezzi condition and can easily be shown to lock. (Note that the order of the velocity interpolation must be at least one degree higher than that of the pressure interpolation in order to satisfy the convergence criteria). Only if the degree of velocity interpolation is increased to quadratic (i.e. the quadratic velocity-constant pressure triangle shown in Fig. 3(b)) can the compressibility (or nearly incompressibility) condition be satisfied. On the other hand, the bilinear velocity-constant pressure quadrilateral element shown in Fig. 3(c) does not lock. This means that quadrilateral elements, compared to triangular elements, allows the use of coarser meshes for a desired accuracy in pressure interpolation. At the same time, the quadrilateral mesh will exhibit fewer nodes which means less computational storage. Also, the quadrilateral element allows optimum rate of convergence compared to the triangular element of Fig. 3(b). For these reasons, it is far more advantageous to use quadrilateral elements compared to triangular elements to solve the incompressible flow problem.

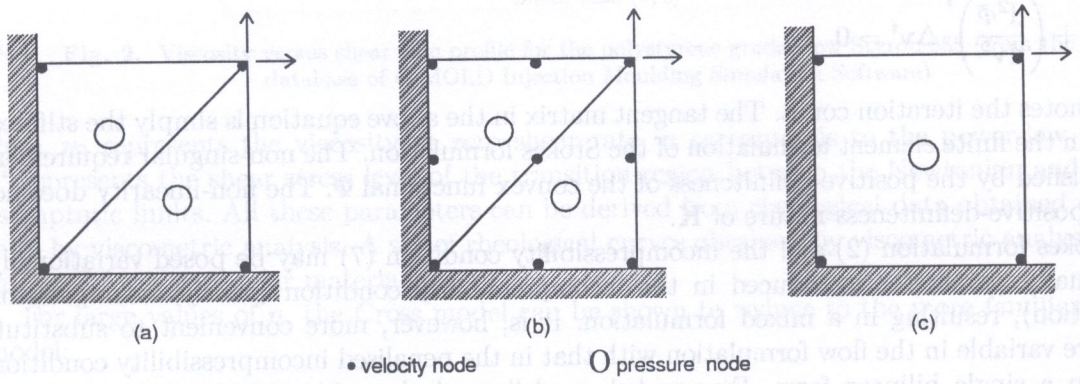

Fig. 3. Various element configurations showing velocity and pressure interpolation nodes

This apparent need for quadrilateral mesh generators lead to the advent of techniques such as *isoparametric mapping and transfinite mapping* for the generation of quadrilaterals. These techniques involve the manual subdivision of the domain into simpler subregions which are then mapped onto regular grids. As the element sizes are controlled by the subregions, these methods are not suitable for adaptive analysis which often requires meshes with vastly differing element sizes.

The method proposed by Zhu *et al.* [14] for the automatic generation of quadrilateral meshes has thus far proved the most computationally viable technique and is suitable for use in adaptive analysis for the generation of optimal meshes. The method is based on the following facts:

- A region can always be subdivided entirely into quadrilaterals if the polygon which forms the boundary of the region has an even number of sides.
- A quadrilateral can be formed by two triangles which form a common side.

These facts, together with the use of the advancing front technique developed for the generation of triangular meshes by Peraire *et al.* [12], are used to develop an algorithm for the generation of quadrilateral meshes. A "background mesh", or the previous mesh, which contains values of nodal densities obtained via adaptive analysis, is used to determine the nodal mesh densities using interpolation methods.

This method has been shown to generate meshes for highly irregular domains with large variations in element size distribution. Also, the fully automatic technique can be used for problems requiring *moving meshes*. Unlike previous grid generation and stretching techniques which were constrained by the number of elements in the initial mesh leading to unacceptable element distortion, this technique can be used to generate entirely new meshes at each iteration or integration step and is therefore suitable for problems with large changes in domain size.

3.3. Free surface (melt front) advancement and solid wall penetration

In advancing the free surface using the predictor

$$\mathbf{x} = \mathbf{v}\Delta t \tag{16}$$

the free surface may penetrate the solid wall boundaries of the domain. Different approaches have been used to counter this. Hieber and Shen [1] used a method in which the time step is reduced by the equivalent distance of encroachment of the free surface displacement vector. For the Hele-Shaw model, this method works well since the fluid slips along the solid walls and encroachment mainly occurs when the flow encounters inside bends or corners. In the Stokes model, the flow near a solid boundary is towards the boundary. Encroachment will therefore occur frequently resulting in very small time steps for fine meshes.

More sophisticated methods have been developed. These include the *boundary pressure reflection method* of Lee *et al.* [37]. This method, developed for the Hele-Shaw model, is based on the iterative adjustment of the pressure at the fluid-solid wall interface until the fluid flux (or pressure gradient) normal to the boundary is zero. The pressure adjustment is based on the pressure drop across the penetrated fluid. This method conserves the mass and therefore does not require any adjustment of the time step. An equivalent method for the Stokes model has not yet been developed. Other methods based on the use of penalty functions have been developed for metal forming problems. These may be adapted for the injection mould filling problem.

The technique used in this study is simply to move any encroached nodes back onto the boundary. The time t is adjusted to account for this flow reduction, thus ensuring mass conservation. The encroachment is detected by searching for the mapped position of each advanced node within the mapped (master) element of each element, using the isoparametric mapping technique.

3.4. The computational algorithm

The computational algorithm to be used in the analysis of planar viscous jets, depicted by the flowchart in Fig. 4, consists of the following sub-algorithms:

- The generation/regeneration of the finite element mesh.
- The nonlinear (Non-Newtonian) solution of the Finite Element flow formulation.
- The explicit advancement of the free surface and the tracking of the solid boundaries.

This is part of a code developed specifically for injection mould filling analysis. Although the features of adaptive mesh refinement and implicit free surface correction are available in the code [10], they will not be employed in the buckling analysis.

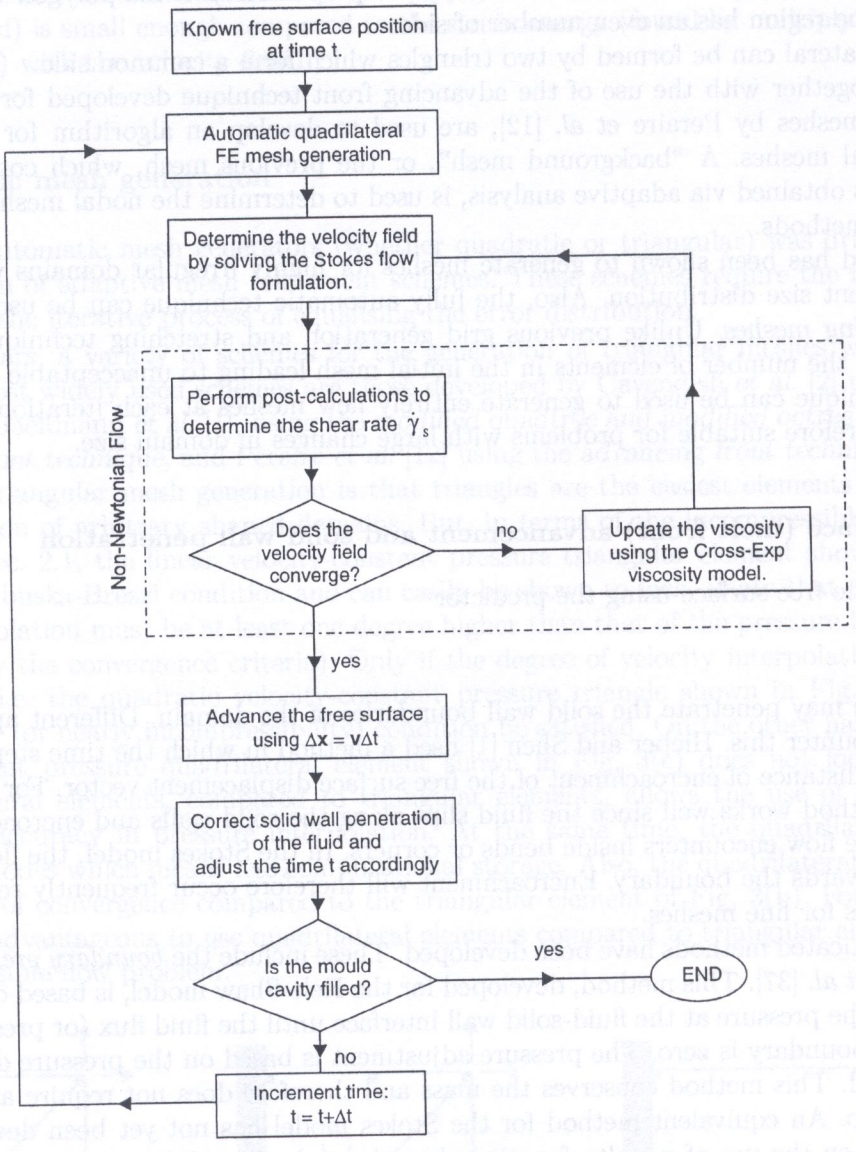

Fig. 4. Flowchart of the computation algorithm used in the analysis

4. Simulation of the Buckling of Newtonian and Non-Newtonian Jets

In the following example, a polymer melt at a temperature of 200°C and with the viscosity characterisation of Fig. 2/Table 1 is injected into the 50mm × 50mm square mould cavity shown in Fig. 5. The gate width is 4 mm giving an aspect ratio $H/D = 12.5$. The Reynolds number for the Newtonian flow can be calculated using the following:

$$\mathrm{Re} = \frac{\mathbf{v}_e D}{\nu_0}$$

where v_e is the uniform inlet velocity and ν_0 is the zero shear-rate kinematic viscosity given by:

$$\nu_0 = \frac{\eta_0}{\rho}.$$

The zero shear rate fluid viscosity η_0 can be calculated using Eq. (12a) together with the values of the Cross constants given in Table 1, giving $\eta_0 = 1.303 \times 10^5$ Pa.s. The density ρ of the polymer

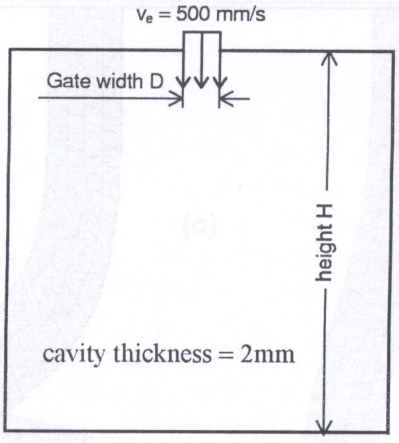

Fig. 5. Mould geometry for the simulation of Newtonian and Non-Newtonian jets

melt can be found by using the well known Tait Model which relates the density (or specific volume) to the pressure and temperature. The details of the model, including the parameters for a polystyrene melt, are presented in references [38, 39]. The effect of pressure on the planar jet is minimal and the density, at 200°C, is found to be 960 kg/m^3. Using these values in the above two equations gives the kinematic viscosity $\nu_0 = 135.7$ m^2/s and the Reynolds number Re $= 1.5 \times 10^{-4}$.

Both the Cruikshank conditions are therefore satisfied for the Newtonian case and the jet is expected to buckle. In the present Stokes flow model, the inertia effects are neglected. However, this will not affect the results because the Reynolds number is extremely low. In the case of Non-Newtonian flow of polymer melts, the Reynolds number is still relatively low. Even in the case of high shear rates, of the order of 10^4 s^{-1}, the fluid viscosity η for the Polystyrene Dow Styron 685 polymer melt at 200°C reduces to about 50 Pa.s. This gives a local Reynolds number Re ≈ 0.4 which still satisfies the Cruikshank condition. The predominant (or effective average) Reynolds number may still be much lower than this value, and the Non-Newtonian jet is also expected to buckle.

The buckling of the Newtonian and Non-Newtonian jets are shown at comparative times in Fig. 6. A constant mesh density of 1 mm is used with a time step of 0.002 seconds. The buckling is initiated by the slight asymmetry in the finite element computations produced by the non-symmetrical mesh. There is no need therefore to introduce an artificial imperfection in the material or a slight skewing of the jet.

It is evident that the Non-Newtonian jet starts to buckle earlier, as seen at $t = 0.14$. This is because the Non-Newtonian jet tends to be narrower, whereas the Newtonian jet tends to bulge outwards, accommodating more fluid. The Newtonian jet forms a wider arch and folds later than the Non-Newtonian jet, as seen at $t = 0.200$. Only the Newtonian jet is shown at $t = 0.240$ because the free surface of the Non-Newtonian jet has already welded.

In the case of lower viscosity fluids, the Non-Newtonian jet is expected to buckle less (or even not at all) compared to the Newtonian jet [13]. This is because the high shear rates near the obstruction lead to greater lateral mobility. Unfortunately, this comparison cannot be illustrated here because the Stokes flow model cannot be used to model the lower viscous (higher Reynolds number) flows.

To test the validity of the Cruikshank aspect ratio condition, the length of the cavity is reduced to 40 mm giving $H/D = 10.0$. The Newtonian jet is still expected to buckle, and this is verified by the results in Fig. 7. In this case, the jet develops wider and tends to offer more resistance to buckling, but the overall performance is similar to that in the previous case. Less folds are expected because of the shorter distance between the gate and the normal obstruction.

The cavity height H is further reduced to 28 mm, giving $H/D = 7.0$. This is below the Cruikshank value of 3π. The corresponding behaviour of the Newtonian jet is shown in Fig. 8. As predicted by the Cruikshank conditions, there is no occurrence of buckling for this case. The Cruikshank

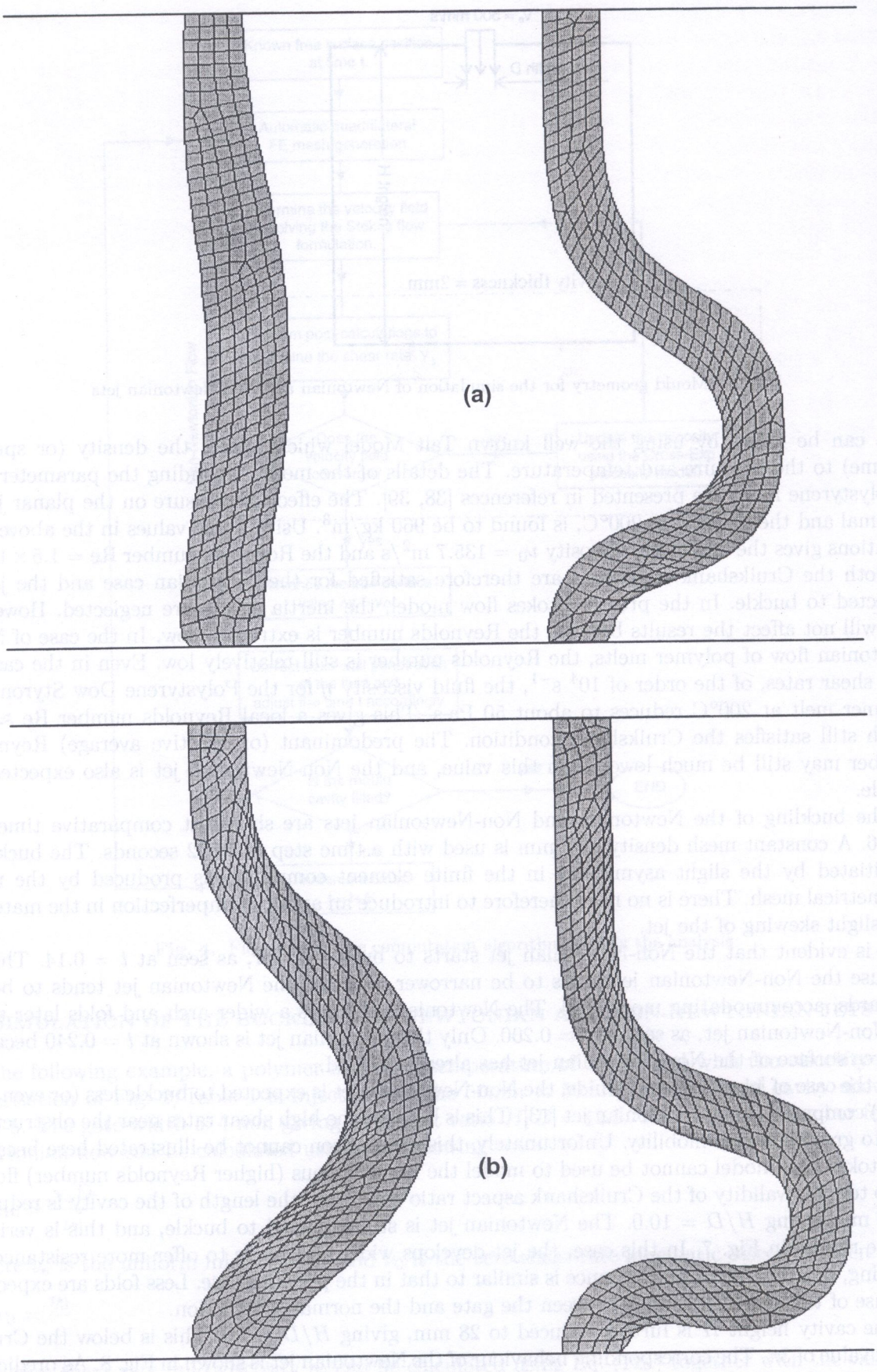

Fig. 6. Buckling of a Newtonian jet (left) and a Non-Newtonian jet (right) for $H/D = 12.5$ at comparative times (a) $t = 0.140$, (b) $t = 0.160$(*continued*)

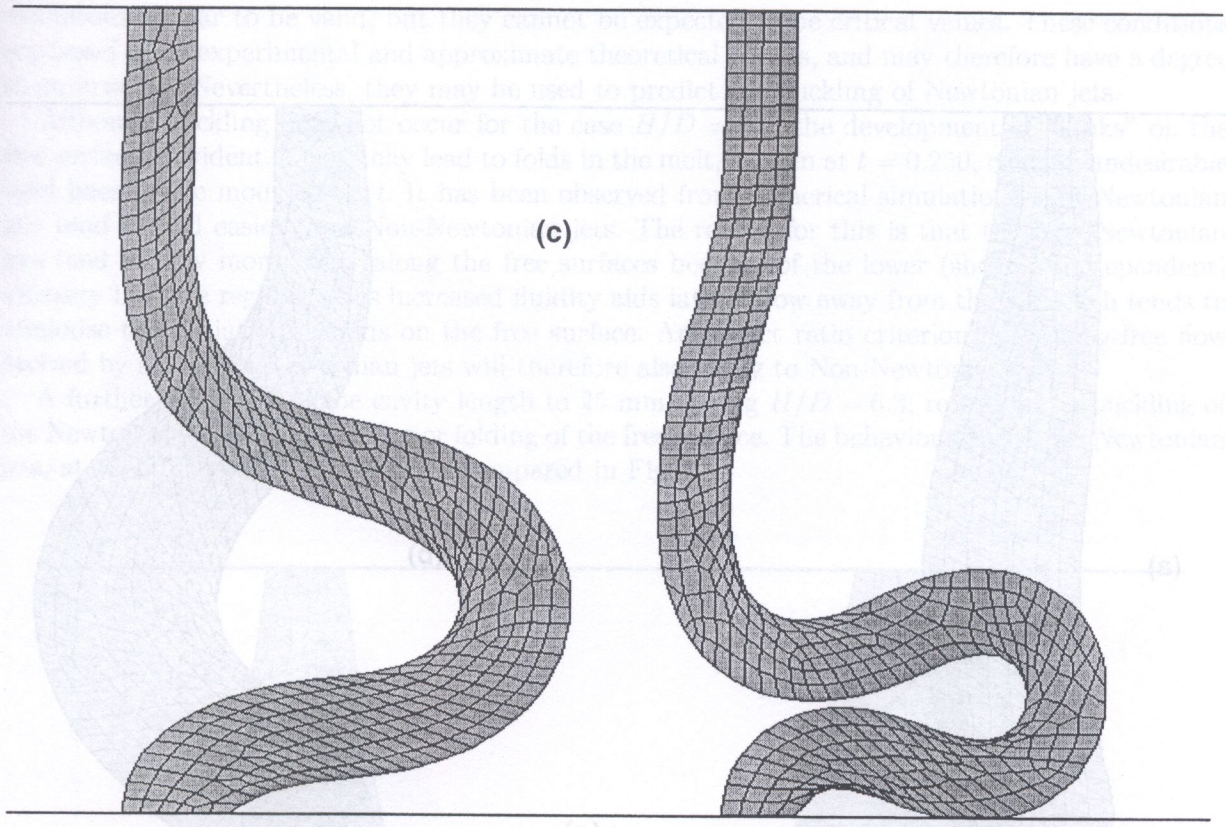

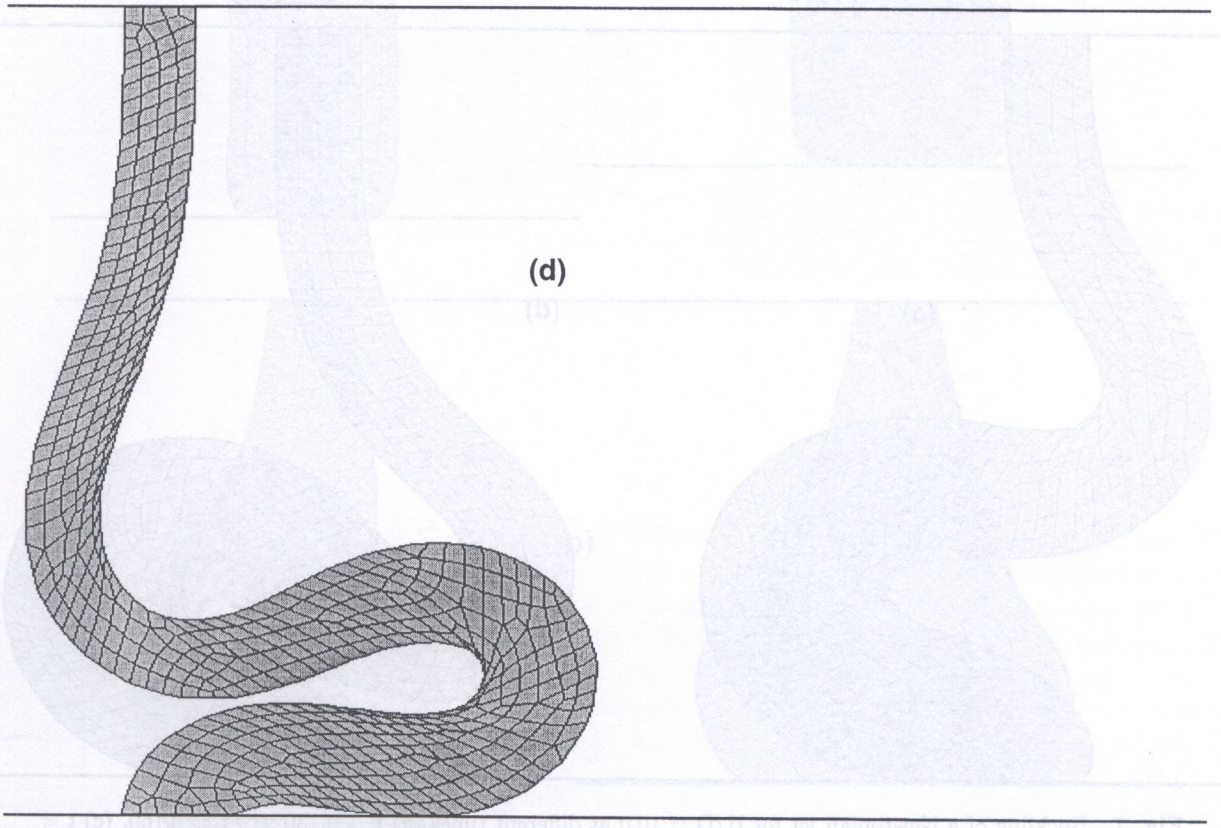

Fig. 6. (*continued*) Buckling of Newtonian jet (left) and a Non-Newtonian jet (right) for $H/D = 12.5$ at comparative times (c) $t = 0.200$, (d) $t = 0.240$

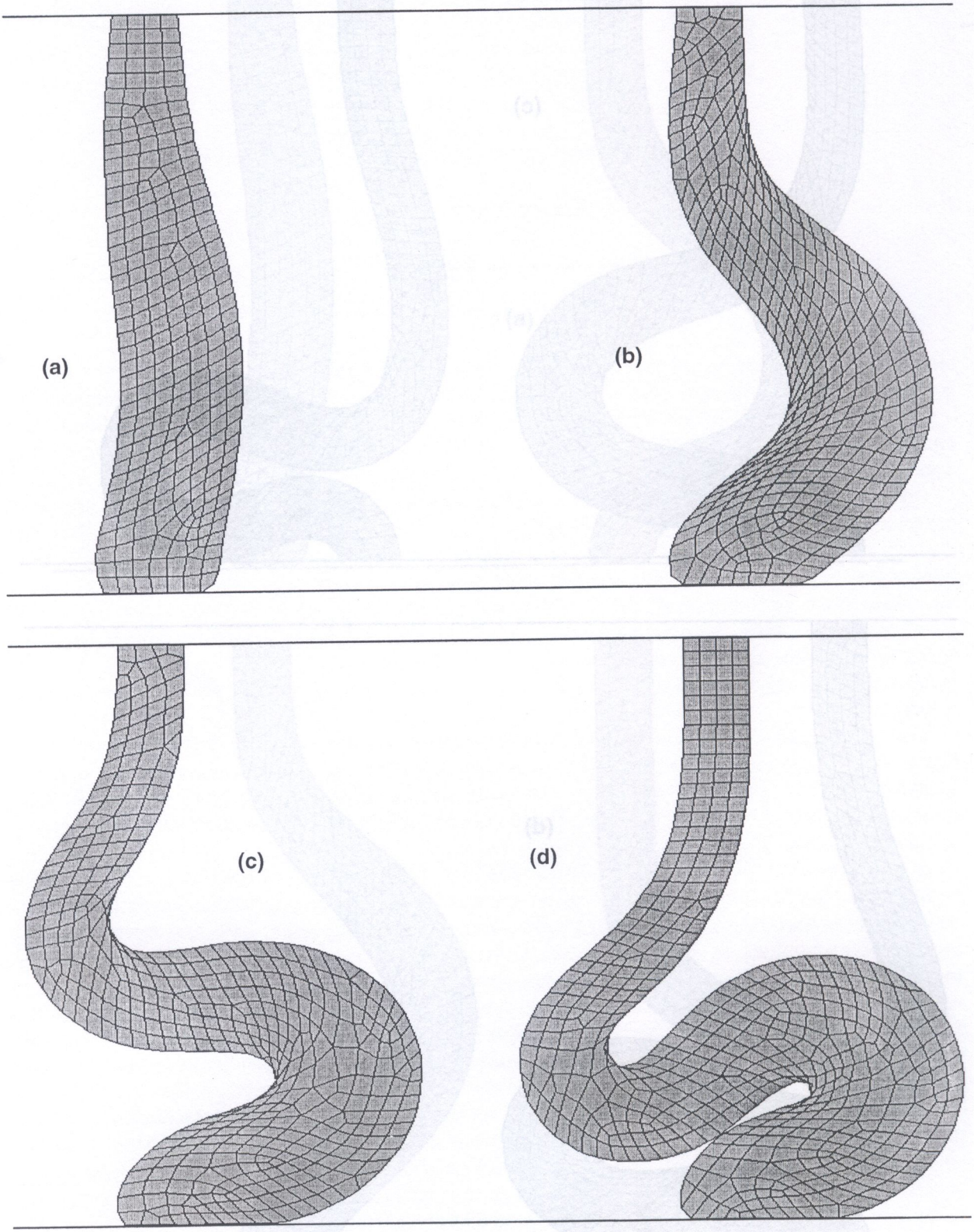

Fig. 7. Buckling of a Newtonian jet for H/D = 10.0 at different times (a) t = 0.130, (b) t = 0.160, (c) t = 0.200, (d) t = 0.240

conditions appear to be valid, but they cannot be expected to be critical values. These conditions are based upon experimental and approximate theoretical results, and may therefore have a degree of uncertainty. Nevertheless, they may be used to predict the buckling of Newtonian jets.

Although buckling does not occur for the case $H/D = 7.0$, the development of "kinks" on the free surface is evident. These may lead to folds in the melt, as seen at $t = 0.250$, causing undesirable weld lines in the moulded part. It has been observed from numerical simulations that Newtonian jets tend to fold easier than Non-Newtonian jets. The reason for this is that the Non-Newtonian jets tend to flow more easily along the free surfaces because of the lower (shear rate dependent) viscosity in these regions. This increased fluidity aids lateral flow away from the jet which tends to minimise the initiation of folds on the free surface. An aspect ratio criterion for folding-free flow derived by analysing Newtonian jets will therefore also apply to Non-Newtonian jets.

A further reduction of the cavity length to 25 mm, giving $H/D = 6.3$, results in no buckling of the Newtonian jet (as expected), nor folding of the free surface. The behaviour of the two Newtonian jets, at $H/D7.0$ and $H/D = 6.3$, are compared in Fig. 8.

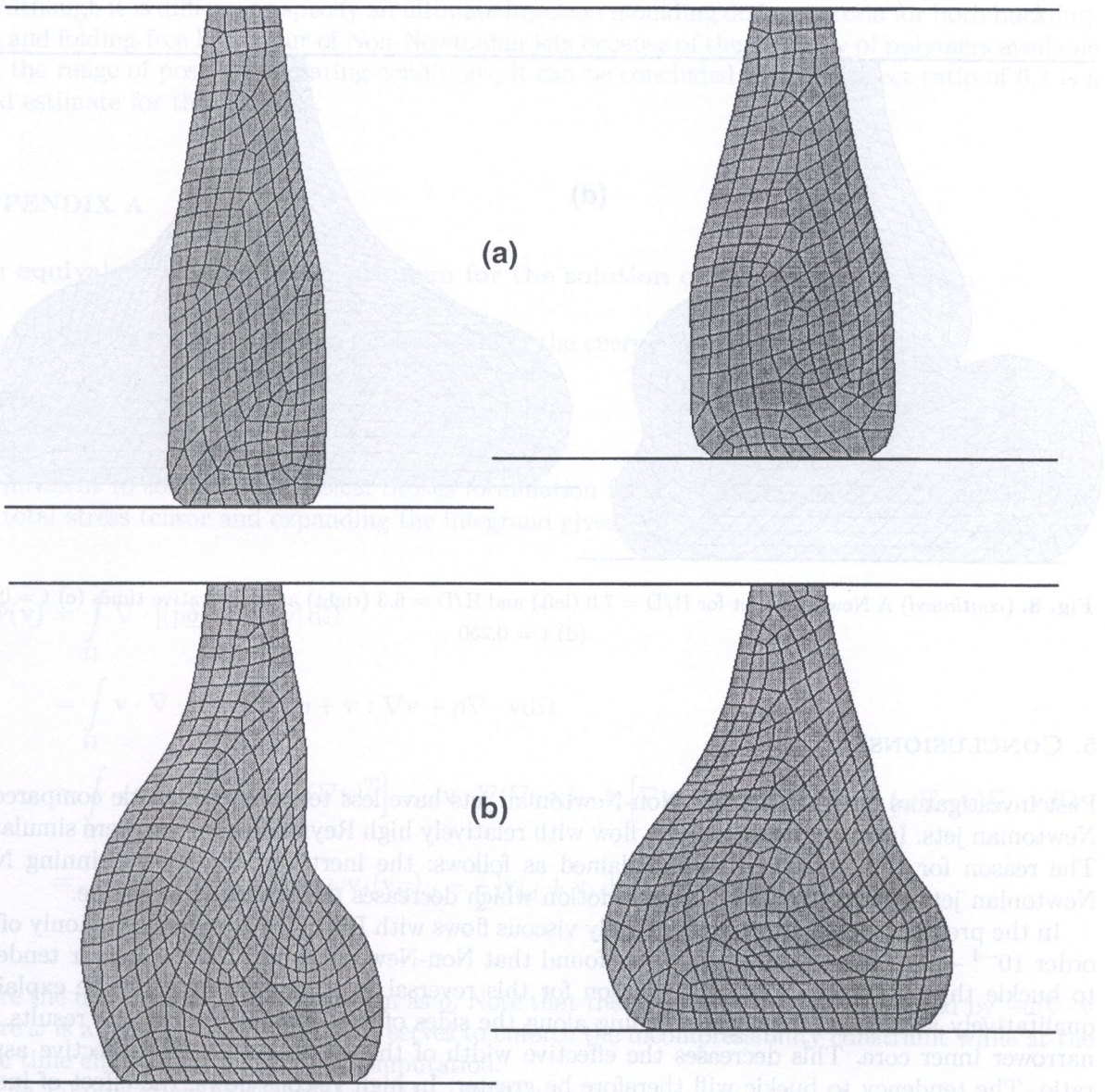

Fig. 8. A Newtonian jet for H/D = 7.0 (left) and H/D = 6.3 (right) at comparative times (a) t = 0.100, (b) t = 0.150 (*continued*)

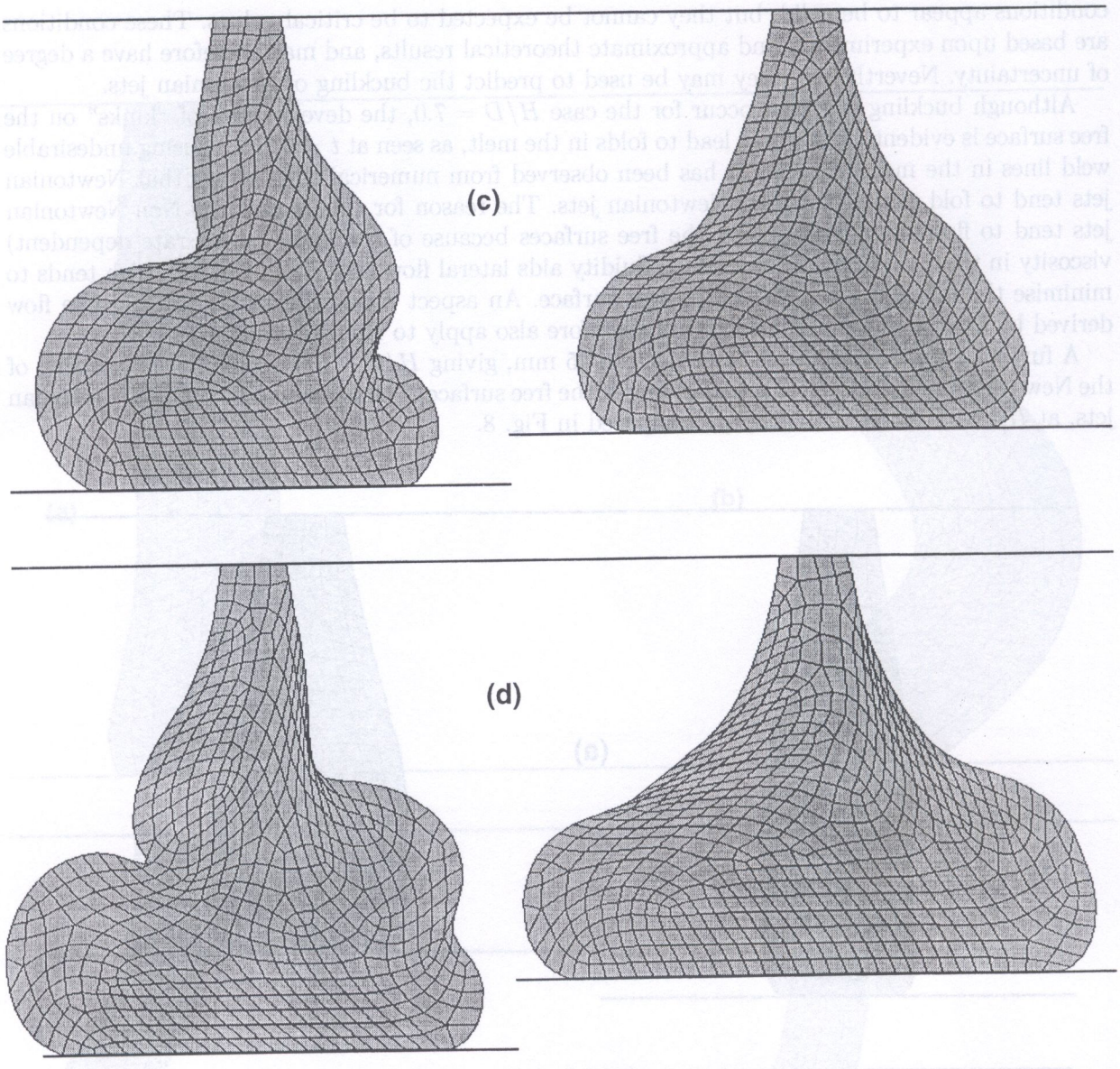

Fig. 8. (*continued*) A Newtonian jet for H/D = 7.0 (left) and H/D = 6.3 (right) at comparative times (c) t = 0.200, (d) t = 0.250

5. Conclusions

Past investigators have shown that Non-Newtonian jets have less tendency to buckle compared to Newtonian jets. In these investigations, flow with relatively high Reynolds numbers were simulated. The reason for this behaviour was explained as follows: the inertia of the shear-thinning Non-Newtonian jets results in greater lateral motion which decreases the tendency to buckle.

In the present investigation, where highly viscous flows with Reynolds numbers commonly of the order $10^{-4} - 10^{-1}$ were simulated, it was found that Non-Newtonian jets have a greater tendency to buckle than Newtonian jets. The reason for this reversal in behaviour can only be explained qualitatively as follows: the shear-thinning along the sides of the Non-Newtonian jets results in a narrower inner core. This decreases the effective width of the jet, increasing the effective aspect ratio. The tendency to buckle will therefore be greater. In high viscous flows, the effect of inertia is negligible, and the lateral expansion of the jet is insufficient to reduce the tendency to buckle.

The Cruikshank conditions were shown to be valid for the case of highly viscous Newtonian jets. In particular, it was shown that the Reynolds number condition is always satisfied for both Newtonian and Non-Newtonian polymeric jets under typical injection moulding conditions. The aspect ratio condition is therefore the critical condition dictating the phenomenon of buckling. However, as discussed previously, the aspect ratio condition for buckling of Newtonian jets cannot be used as an injection moulding design criteria where Non-Newtonian behaviour is present. This will depend on the particular polymer used and should be lower than the value of 3π specified by the Cruikshank condition.

It was shown in the case of Newtonian jets that, although buckling does not occur for aspect ratios below 3π, folds on the free surface may still develop resulting in undesirable welding of the polymeric fluid. In fact, an aspect ratio of approximately 6.3 (or 2π) was shown to produce buckling-free and folding-free behaviour of Newtonian jets.

It was observed that the shear-thinning Non-Newtonian jets have a lower tendency to develop folds on the free surface. The reason for this is that the increased fluidity along the free surface tends to iron out any kinks and prevents the initiation of folds. A design criteria against free surface folding based on Newtonian behaviour will therefore suffice for the case of Non-Newtonian jets.

Although it is difficult to specify an ultimate injection moulding design criteria for both buckling-free and folding-free behaviour of Non-Newtonian jets because of the diversity of polymers available and the range of possible operating conditions, it can be concluded that an aspect ratio of 6.3 is a good estimate for this purpose.

APPENDIX A

An equivalent minimisation problem for the solution of the Stokes problem

The aim here is to show that the minimisation of the energy functional

$$\Phi(\mathbf{v}) = \int_{\Omega} \nabla \cdot (\boldsymbol{\pi} \cdot \mathbf{v}) \mathrm{d}\Omega$$

is equivalent to solving the classical Stokes formulation for some fixed domain Ω. Substituting for the total stress tensor and expanding the integrand gives

$$\begin{aligned}
\Phi(\mathbf{v}) &= \int_{\Omega} \nabla \cdot [(p\underline{\delta} + \boldsymbol{\tau}) \cdot \mathbf{v}] \, \mathrm{d}\Omega \\
&= \int_{\Omega} \mathbf{v} \cdot \nabla \cdot \boldsymbol{\tau} + \mathbf{v} \cdot \nabla p + \boldsymbol{\tau} : \nabla \mathbf{v} + p \nabla \cdot \mathbf{v} \mathrm{d}\Omega \\
&= \int_{\Omega} -\eta \mathbf{v} \cdot \nabla \cdot \left[\nabla \mathbf{v} + (\nabla \mathbf{v})^T \right] - \omega \mathbf{v} \cdot \nabla (\nabla \cdot \mathbf{v}) - \eta \left[\nabla \mathbf{v} + (\nabla \mathbf{v})^T \right] : \nabla \mathbf{v} - (\omega \nabla \cdot \mathbf{v}) \nabla \cdot \mathbf{v} \mathrm{d}\Omega \\
&= \int_{\Omega} -\eta \mathrm{v}_j \left[\mathrm{v}_{ij} + \mathrm{v}_{ij} \right]_j - \omega \mathrm{v}_j (\mathrm{v}_{ij})_{,j} - \frac{\eta}{2} \left[\mathrm{v}_{i,j} + \mathrm{v}_{j,i} \right] \left[\mathrm{v}_{i,j} + \mathrm{v}_{j,i} \right] - \omega \mathrm{v}_{i,j} \mathrm{v}_{j,i} \mathrm{d}\Omega
\end{aligned}$$

where the unit tensor has been written as $\underline{\delta}$. Note that the pressure p has been replaced by $-\omega \nabla \cdot \mathbf{v}$ where ω is a penalty parameter. This serves to enforce the incompressibility constraint while at the same time eliminating p from the computation.

The minimisation of Φ implies setting its first variation to zero. The first variation of Φ is given by:

$$\delta\Phi = \int_\Omega -\eta\delta\mathrm{v}_j\left[\mathrm{v}_{i,j}+\mathrm{v}_{j,i}\right]_{,j} - \eta\mathrm{v}_j\delta\left[\mathrm{v}_{i,j}+\mathrm{v}_{j,i}\right]_{,j} - \omega\delta\mathrm{v}_j(\mathrm{v}_{i,j})_{,j} - \omega\mathrm{v}_j\delta(\mathrm{v}_{i,j})_{,j}$$

$$-\frac{\eta}{2}2\delta\left[\mathrm{v}_{i,j}+\mathrm{v}_{i,j}\right]\left[\mathrm{v}_{i,j}+\mathrm{v}_{j,i}\right] - \omega\delta(\mathrm{v}_{i,i})\mathrm{v}_{j,j} - \omega\mathrm{v}_{i,i}\delta(\mathrm{v}_{j,j})\mathrm{d}\Omega$$

$$= \int_\Omega -\eta\delta\mathrm{v}_j\left[\mathrm{v}_{i,j}+\mathrm{v}_{j,i}\right]_{,j} - \eta\mathrm{v}_j\delta\left[\mathrm{v}_{i,j}+\mathrm{v}_{j,i}\right]_{,i} - \omega\delta\mathrm{v}_j(\mathrm{v}_{i,i})_{,j} - \omega\mathrm{v}_j\delta(\mathrm{v}_{i,i})_{,j}$$

$$-\eta\delta(\mathrm{v}_{i,j})\left[\mathrm{v}_{i,j}+\mathrm{v}_{j,i}\right] - \eta\delta(\mathrm{v}_{j,i})\left[\mathrm{v}_{i,j}+\mathrm{v}_{j,i}\right] - \omega\delta(\mathrm{v}_{i,i})\mathrm{v}_{j,j} - \omega\mathrm{v}_{i,i}\delta(\mathrm{v}_{j,j})\mathrm{d}\Omega$$

Integrating the last four terms by parts gives

$$\delta\Phi = \int_\Omega -\eta\delta\mathrm{v}_j\left[\mathrm{v}_{i,ji}+\mathrm{v}_{j,ii}\right] - \eta\mathrm{v}_j\delta\left[\mathrm{v}_{i,ji}+\mathrm{v}_{j,ii}\right] - \omega\delta\mathrm{v}_j(\mathrm{v}_{i,ij}) - \omega\mathrm{v}_j\delta(\mathrm{v}_{i,ij})$$

$$+\eta\delta\mathrm{v}_i\left[\mathrm{v}_{i,jj}+\mathrm{v}_{j,ij}\right] + \eta\delta\mathrm{v}_j\left[\mathrm{v}_{i,ji}+\mathrm{v}_{j,ii}\right] + \omega\delta\mathrm{v}_i(\mathrm{v}_{j,ji}) + \omega\mathrm{v}_{i,ij}\delta\mathrm{v}_j\mathrm{d}\Omega$$

$$+\int_\Gamma \eta\delta\mathrm{v}_i\mathrm{n}_j\left[\mathrm{v}_{i,j}+\mathrm{v}_{j,i}\right] + \eta\delta\mathrm{v}_j\mathrm{n}_i\left[\mathrm{v}_{i,j}+\mathrm{v}_{j,i}\right] + \omega\delta\mathrm{v}_i\mathrm{n}_i(\mathrm{v}_{j,j}) + \omega\mathrm{n}_j\mathrm{v}_{i,i}\delta\mathrm{v}_j\mathrm{d}\Gamma$$

$$= \int_\Omega -\eta\mathrm{v}_j\delta\left[\mathrm{v}_{i,ji}+\mathrm{v}_{j,ii}\right] - \omega\mathrm{v}_j\delta(\mathrm{v}_{i,ij})) + \eta\delta\mathrm{v}_i\left[\mathrm{v}_{i,jj}+\mathrm{v}_{j,ij}\right] + \omega\delta\mathrm{v}_i\mathrm{v}_{j,ji}\mathrm{d}\Omega$$

$$+\int_\Gamma 2\eta\delta\mathrm{v}_i\mathrm{n}_j\left[\mathrm{v}_{i,j}+\mathrm{v}_{j,i}\right] + 2\omega\delta\mathrm{v}_i(\mathrm{n}_i\mathrm{v}_{j,j})\mathrm{d}\Gamma$$

$$= \int_\Omega -\delta(\eta\left[\mathrm{v}_{i,ji}+\mathrm{v}_{j,ii}\right] + \omega(\mathrm{v}_{i,ij}))\mathrm{v}_j + (\eta\left[\mathrm{v}_{i,jj}+\mathrm{v}_{j,ij}\right] + \omega\mathrm{v}_{j,ji})\delta\mathrm{v}_i\mathrm{d}\Omega$$

$$+\int_\Gamma 2(\eta\mathrm{n}_j\left[\mathrm{v}_{i,j}+\mathrm{v}_{j,i}\right] + \omega\mathrm{n}_i\mathrm{v}_{j,j})\delta\mathrm{v}_i\mathrm{d}\Gamma$$

where n_i are the components of the unit outward normal on the boundary. Rewriting the above equation in non-index form gives:

$$\delta\Phi = \int_\Omega -\delta(\nabla\cdot\eta\left[\nabla\mathbf{v}+(\nabla\mathbf{v})^T\right] + \nabla(\omega\nabla\cdot\mathbf{v}))\cdot\mathbf{v} + (\nabla\cdot\eta\left[\nabla\mathbf{v}+(\nabla\mathbf{v})^T\right] + \nabla(\omega\nabla\cdot\mathbf{v}))\cdot\delta\mathbf{v}\mathrm{d}\Omega$$

$$+\int_\Gamma 2\mathbf{n}\cdot(\eta\left[\nabla\mathbf{v}+(\nabla\mathbf{v})^T\right] + \omega\nabla\cdot\mathbf{v}))\cdot\delta\mathbf{v}\mathrm{d}\Gamma$$

$$= \int_\Omega -\delta(\nabla\cdot(\boldsymbol{\tau}+p\underline{\boldsymbol{\delta}}))\cdot\mathbf{v}\cdot(\boldsymbol{\tau}+p\underline{\boldsymbol{\delta}}))\cdot\delta\mathbf{v}\mathrm{d}\Omega + \int_\Gamma 2\mathbf{n}\cdot(\boldsymbol{\tau}+p\underline{\boldsymbol{\delta}})\cdot\delta\mathbf{v}\mathrm{d}\Gamma$$

$$= \int_\Omega -\delta(\nabla\cdot\boldsymbol{\pi})\cdot\mathbf{v} + (\nabla\cdot\boldsymbol{\pi})\cdot\delta\mathbf{v}\mathrm{d}\Omega + \int_\Gamma 2\mathbf{n}\cdot\boldsymbol{\pi}\cdot\delta\mathbf{v}\mathrm{d}\Gamma$$

Since the variation of velocity is arbitrary in Ω and imposed as zero on Γ, and since the domain of integration is arbitrary, the non-trivial solution is given by

$$\delta\Phi = 0 \Leftrightarrow \begin{cases} \nabla\cdot\boldsymbol{\pi} = \mathbf{0} & \text{on } \Omega \quad (A.1) \\ \mathbf{n}\cdot\boldsymbol{\pi} = \overline{\boldsymbol{\pi}}_n \quad \text{or} \quad \mathbf{v} = \overline{\mathbf{v}} & \text{on } \Gamma \quad (A.2) \end{cases}$$

Equation (A.1) implies that the minimisation of the functional Φ is equivalent to solving the classical Stokes formulation, subject to the boundary conditions (A.2).

Acknowledgements

The first author would like to thank the Foundation for Research Development, South Africa, for their financial support.

References

[1] P.L. Baehmann, S.L. Wittchen, M.S. Shepard, K.R. Grice and M.A. Yerry. Robust geometrically based automatic two-dimensional mesh generation, *Int. J. Num. Meth. Eng.*, **24**: 1043–1078, 1987.

[2] J.C. Cavendish, D.A. Field and W.H. Frey. An approach to automatic three dimensional finite element mesh generation, *Int. J. Num. Meth. Eng.*, **21**: 329–347, 1985.

[3] H.H. Chiang, C.A. Hieber and K.K. Wang. A unified simulation of the filling and postfilling stages in injection molding. Part I: Formulation, *Polym. Eng. Sci.*, V **31**(2): 116–124, 1991.

[4] H.H. Chiang, C.A. Hieber and K.K. Wang. A unified simulation of the filling and postfilling stages in injection molding. Part II: Experimental Verification, *Polym. Eng. Sci.*, V **31**(2): 125–139, 1991.

[5] J.O. Cruikshank. Low-Reynolds-number instabilities in stagnating jet flows, *J. Fluid Mech*, **193**: 111–127, 1988.

[6] C.A. Hieber, S.F. Shen. A finite element/finite difference simulation of the injection moulding filling process, *J. Non-Newt. Fluid Mech.*, **7**: 1–32, 1980.

[7] T.J.R. Hughes. *The Finite Element Method*, Prentice-Hall, 1987.

[8] H.S. Lee, H.C. Sin and S.G. Kim. Iterative boundary pressure reflection method for the simulation of injection mould filling, *Polym. Eng. Sci.*, **30**: 1513–1522, 1990.

[9] S.H. Lo. A new mesh generation scheme for arbitrary planar domains, *Int. J. Num. Meth. Eng.*, **21**: 1403–1426, 1985.

[10] N. Mahomed. Computational Modelling of Injection Mould Filling with a New Treatment of Free Surfaces, *PhD Dissertation*, IPPT, Polish Academy of Sciences, 1997.

[11] K-I. Mori, D. Osakada and S. Takaoka. Simplified three-dimensional simulation of non-isothermal filling in metal injection moulding by the finite element method, *Engineering Computations*, **13**: 111–121, 1996.

[12] J. Peraire, M. Vahdati, K. Morgan and O.C. Zienkiewicz. Adaptive remeshing for compressible flow computations, *J. Comput. Physics*, **72**: 449–466, 1987.

[13] M.F. Tomé, B. Duffy and S. McKee. A numerical technique for solving unsteady non-Newtonian free surface flows, *J. Non-Newtonian Fluid Mech.*, **62**: 9–34, 1996.

[14] J.Z. Zhu, O.C. Zienkiewicz, E. Hinton and J. Wu. A new approach to the development of automatic quadrilateral mesh generation, *Int. J. Num. Meth. Eng.*, **32**: 849–866, 1991.